Chaos ARTICLE scitation.org/journal/cha

Nonlocal Raman response in Kerr resonators: Moving temporal localized structures and bifurcation structure

Cite as: Chaos **30**, 083111 (2020); doi: 10.1063/5.0007350
Submitted: 26 March 2020 · Accepted: 13 July 2020 ·
Published Online: 3 August 2020

M. G. Clerc,[1] S. Coulibaly,[2,a)] P. Parra-Rivas,[3] and M. Tlidi[4]

AFFILIATIONS

[1]Departamento de Física and Millennium Institute for Research in Optics, Facultad de Ciencias Físicas y Matemáticas, Universidad de Chile, Casilla 487-3, Santiago, Chile
[2]Univ. Lille, CNRS, UMR 8523 - PhLAM - Physique des Lasers Atomes et Molécules, F-59000 Lille, France
[3]OPERA-photonique, Université libre de Bruxelles, 50 Avenue F. D. Roosevelt, CP 194/5, B-1050 Bruxelles, Belgium
[4]Faculté des Sciences, Université Libre de Bruxelles (U.L.B), CP 231, Campus Plaine, B-1050 Bruxelles, Belgium

Note: This article is part of the Focus Issue, Instabilities and Nonequilibrium Structures.
[a)]**Author to whom correspondence should be addressed:** saliya.coulibaly@univ-lille.fr

ABSTRACT

A ring resonator made of a silica-based optical fiber is a paradigmatic system for the generation of dissipative localized structures or dissipative solitons. We analyze the effect of the non-instantaneous nonlinear response of the fused silica or the Raman response on the formation of localized structures. After reducing the generalized Lugiato–Lefever to a simple and generic bistable model with a nonlocal Raman effect, we investigate analytically the formation of moving temporal localized structures. This reduction is valid close to the nascent bistability regime, where the system undergoes a second-order critical point marking the onset of a hysteresis loop. The interaction between fronts allows for the stabilization of temporal localized structures. Without the Raman effect, moving temporal localized structures do not exist, as shown in M. G. Clerc, S. Coulibaly, and M. Tlidi, Phys. Rev. Res. **2**, 013024 (2020). The detailed derivation of the speed and the width associated with these structures is presented. We characterize numerically in detail the bifurcation structure and stability associated with the moving temporal localized states. The numerical results of the governing equations are in close agreement with analytical predictions.

Optical nonlinear resonators constitute an excellent platform for researchers. These simple and robust devices display rich dynamics that open fundamental questions and also lead to practical applications. An example is the recent advance in frequency-comb generation in microresonators operating close to the cavity resonance. We investigate the nonlocal-delayed Raman response in optical resonators subject to optical injection. The time-delayed nonlocal response appears in many areas of nonlinear science, such as magnetism, optics, and population dynamics. This phenomenon is a rule rather than an exception. We show that a time-delayed nonlocal response can generate traveling localized structures. We enlighten this mechanism on the generic bistable model through analytical and numerical investigations. Numerical results show a reasonably good agreement with the theoretical predictions. A characterization of the bifurcation structure of traveling localized structures is provided. Furthermore, we propose an experimentally relevant optical device to demonstrate the feasibility of this mechanism that may lead to proper new research in Kerr-comb-based devices.

I. INTRODUCTION

The laser field confined in nonlinear optical resonators is modeled by the paradigmatic Lugiato–Lefever Equation (LLE[1]). This simple model constitutes an excellent tool for the understanding and analysis of various intra-cavity behaviors such as localized structures,[2,3] fronts,[4,5] spatiotemporal chaos,[6,7] and rogue waves[8,9] (see recent overviews on the theory and applications of the LLE[10,11]). In particular, localized structures (LSs), often called dissipative solitons or cavity solitons, are the most studied nonlinear object. They can be classified into two categories, spatial and/or temporal. This

is a well documented issue of nonlinear science, such as chemistry, plant ecology, and optics.[12,13] In the temporal regime, they consist of a single stable pulse or more pulses on top of a low intensity background.[2,3] Recently, considerable attention has been devoted both from a fundamental as well as from an applied point of view. From a theoretical point of view, temporal LSs undergo a rich dynamical behavior such as multi-stability, self-pulsing, spatiotemporal chaos, or chimera state propagation along chains of coupled resonators.[14] From an applied point of view, it is worth mentioning recent breakthroughs in frequency-comb generation in microresonators[15–18] when pumped close to the cavity resonance condition.

Recently, the mean-field model, which consists of the LLE[1] with the Raman delayed nonlocal response,[19] has been shown to support moving temporal LSs.[20] Note that local delay feedback can induce spontaneously the motion of LSs.[21–23] The dynamics of macroscopic systems is often subjected to time-delayed feedback. This effect originates from temporal correlations that are inherent not only to optical[24,25] but also to magnetic[26] and biological systems.[27–30]

In the present work, we focus on the normal dispersion regime where homogeneous steady states (HSSs) are modulationally stable, i.e., far from any symmetry-breaking instability. More precisely, we focus on the understanding of moving LSs formation in a generic bistable model that has been recently derived, together with the law governing the interaction between two well-separated fronts.[20] In this contribution, we provide a detailed derivation of this law. This interaction allows the stabilization of moving LSs under the influence of the Raman response. More importantly, we compute the bifurcation and phase diagrams associated with these structures under the influence of the Raman response and highlight the connection between such bifurcation structure and the front interaction and locking. To construct these diagrams, we apply numerical parameter continuation algorithms based on a Newton–Raphson solver.[51,52]

Our results can be applied to optical frequency-comb generators such as all-fiber resonators, whispering-gallery-mode resonators, or microresonators with the Raman effect. Frequency combs generated in optical Kerr resonators can be seen as the spectral content of the stable LS occurring in the cavity. This link has been discussed (see recent review[31] in the theme issue[32]). Besides their impact on fundamental physics, optical frequency combs have led to significant advances in many real-life applications, such as precision distance measurements, optical waveform, and microwave synthesis, and optical spectroscopy.[15–18]

The paper is organized as follows. In Sec. II, we review the LLE with the Raman response and present the reduced generic bistable model with a Raman term. This reduction is valid close to the critical point associated with bistability. This approach allows us to develop a simple and clear analytical description of the front interaction leading to the stabilization of moving LSs with a nonlocal delayed term. The interaction law between two well-separated fronts has been established recently.[20] A detailed derivation of the interaction law between two fronts is provided in Sec. III. This completes our recent communication[20] on this issue. Through a front interaction approach, we characterize moving temporal LSs by calculating their shape, width, and speed. We show that fronts interaction impacts drastically the dynamics of these structures. In Sec. IV, we study the bifurcation structure and stability of the LSs formed through front interaction and locking. This numerical study completes the previous analytical work and allows us to determine the regions of the existence of such states, allowing a classification. Finally, in Sec. V, we present our main conclusions.

II. DESCRIPTION OF THE MODEL

We consider all-fiber ring cavities coherently driven by an injected light beam as shown in Fig. 1. The envelope of the electric field circulating inside the optical cavity is described by the LLE[1] with the Raman delayed nonlocal response[19]

$$\frac{\partial A}{\partial \zeta} = S - (1 + i\Delta)A - ib_2\frac{\partial^2 A}{\partial T^2} + i\left(1 - f_R\right)|A|^2 A + iaf_R A\int_{-\infty}^{T} \chi(T - T')|A(T')|^2\, dT'. \quad (1)$$

Here, $A = A(\zeta, T)$ is the normalized mean-field cavity electric field and Δ accounts for the normalized detuning parameter and losses are normalized to unity. Time ζ is the slow time describing the evolution over successive round trips, and T is the fast time in the reference frame moving with the group velocity of the light within the cavity. S is the input field amplitude, and b_2 the second-order chromatic dispersion coefficient. The Raman effect is described by an integral whose strength is f_R and $a = \tau_0(\tau_1^2 + \tau_2^2)/(\tau_1\tau_2^2)$. The delay kernel function $\chi(\tau)$ is $\chi(\tau) = \exp(-\tau_0\tau)/\tau_2 \sin(\tau_0\tau/\tau_1)$, with $\tau_0 = [|b_2 L|/2\alpha_c]^{1/2}$, where α_c is the losses parameter. The choice of this Kernel, or influence function, has been proposed in Refs. 33 and 34 and shows an excellent agreement with experiments

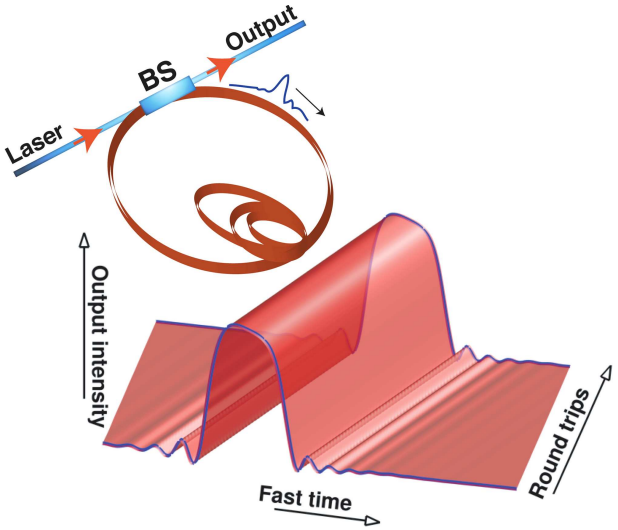

FIG. 1. Schematic representation of a fiber ring cavities coherently driven by an injected light beam and spatiotemporal evolution in the $\zeta - T$ map of a pulse obtained using model Eq. (1) obtained for $\Delta = 4$, $\tau_0 = 5$ fs, $S_1 = 2.202$, ($S_2 = 2.223$), $f_R = 0.18$, $\tau_1 = 12$ fs, $b_2 = 1$, and $\tau_2 = 32$ fs.

using standard fiber. In the absence of Raman effect, i.e., $f_R = 0$, fronts,[4] motionless LS connecting HSS solutions, and moving LSs due to the third-order dispersion effect[35–38] have been reported. In the spatial domain, where chromatic dispersion is replaced by diffraction, the motion of LSs can be triggered by the nonlinear gradient term in the cubic complex Ginzburg-Landau.[39,40]

In what follows, we focus on the nascent optical bistability regime originated at the critical point defined by $\Delta_c = \sqrt{3}$, $A_c = (3 - i\sqrt{3})S_c/4 = A_{rc} + iA_{ic}$, where $S_c^2 = 8\sqrt{3}/9$ is the value of the injected field at criticality. Starting from Eq. (1), the deviation $u \equiv A_r - A_{rc}$ of the electric field envelope from its value at the onset of bistability is shown to obey the generic bistable model[20]

$$\partial_t u = \eta + \mu u - u^3 + D\partial_{\tau\tau} u + \int_{-\infty}^{\tau} \chi(\tau - \tau')u(\tau')\, d\tau', \quad (2)$$

where $u = u(t, \tau)$ is a scalar order parameter and the delay kernel function $\chi(\tau)$ reads

$$\chi(\tau) = \frac{2af_R}{3} e^{\frac{-\tau_0 \tau}{\tau_2}} \sin(\tau_0 \tau/\tau_1) \quad (3)$$

In the limit of large τ_1 and τ, Eq. (2) can be approximated by

$$\partial_t u = \eta + \mu u - u^3 + D\partial_{\tau\tau} u + \gamma\alpha \int_{-\infty}^{\tau} e^{-\alpha(\tau-\tau')} u(\tau')\, d\tau', \quad (4)$$

where $\alpha = \tau_0/\tau_2$ and $\gamma = 2\tau_1 f_R/(3\tau_2)$ account for the characteristic correlation time and the strength of the nonlocal delayed response, respectively. The above model corresponds to the universal model of bistability, *the imperfect pitchfork bifurcation normal form*, plus a nonlocal coupling term that accounts for the Raman effect. Note that exponential nonlocal delay is the most common kernel used in neuroscience.[30]

The HSS solution u_0 satisfies

$$\eta = -(\mu + \gamma)u_0 + u_0^3,$$

which depends on the strength of time-delayed nonlocal response, i.e., γ. In the bistable regime (i.e., for $\mu + \gamma > 0$), three solution branches u_b, u_m, and u_t coexist. The region of coexistence is limited by the folds or saddle-node bifurcations SN_b and SN_t occurring at $u_0^b = \sqrt{\mu + \gamma}/3$ and $u_0^t = -\sqrt{\mu + \gamma}/3$, respectively.

In the absence of the Raman effect, Eq. (4) possess a Lyapunov functional

$$\partial_t u = -\partial_u V(u) \quad \text{with} \quad V(u) = -\eta u - \mu u^2/2 + u^4/4. \quad (5)$$

At the Maxwell point, i.e., $\eta = 0$, Eq. (4) admits exact nonlinear front solutions

$$u_\pm(\tau) = \pm\sqrt{\mu}\tanh[\sqrt{\mu/2}(\tau - \tau_p)], \quad (6)$$

where

$$\tau_p \equiv \int_{-\infty}^{\infty} \tau\partial_\tau u_\pm(\tau)\, d\tau \Big/ \int_{-\infty}^{\infty} \partial_\tau u_\pm(\tau)\, d\tau \quad (7)$$

is the front position. The front solution $u_\pm$ is indexed by "+" and "−" that account, respectively, for the increasing and decreasing monotonous solution as a function of τ. Examples of such types of solutions are shown in Figs. 2(a) and 2(b) at the Maxwell point ($\eta = 0$) and just below it ($\eta = -0.03$), respectively. When $\eta \neq 0$, the front drifts with a constant speed as shown in Fig. 2(b).

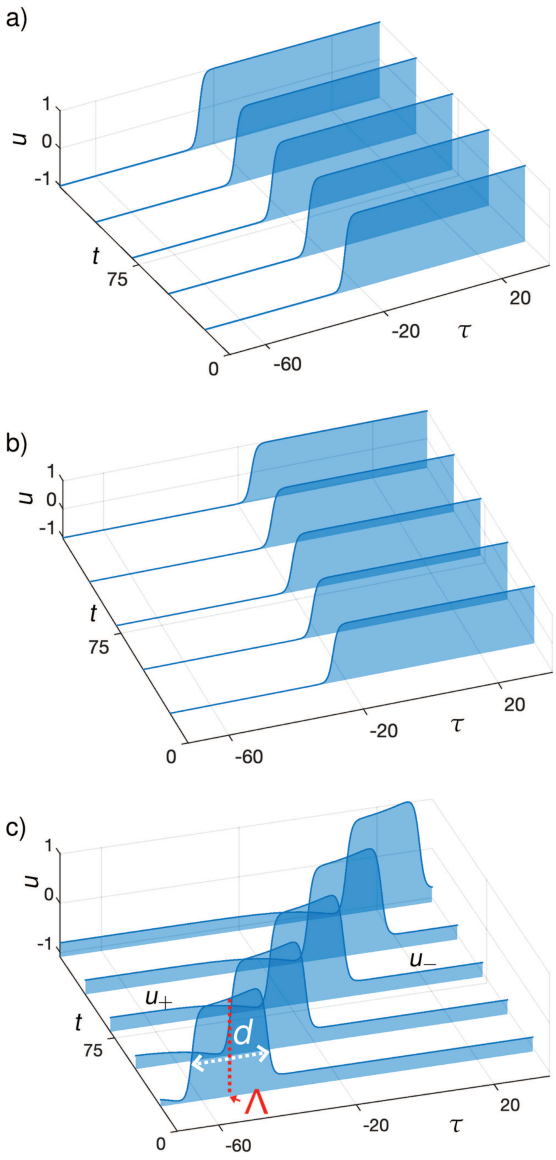

FIG. 2. (a) Front profile and spatiotemporal evolution at the Maxwell point $\gamma = 0$, $\alpha = 0.1$, $\mu = 1$, and $\eta = 0$. (b) Front profile and spatiotemporal evolution with $\gamma = 0$, $\alpha = 0.1$, $\mu = 1$, and $\eta = -0.03$. (c) Pulse propagation with $\gamma = -0.4$, $\alpha = 0.1$, $\mu = 1$, and $\eta = -0.03$. Schematic representation of the interaction of fronts. d and Λ account for the width and centroid between fronts. u_+ and u_- stand for the increasing and decreasing front, respectively.

III. FRONT INTERACTION

Due to the Raman effect, and when two fronts are well-separated from each other, they interact through their overlapping tails. We shall see that the nature of the interaction is

strongly affected by the Raman response leading to the stabilization of traveling LSs like those shown in Fig. 2(c), which otherwise are excluded.[20]

To describe the interaction between two fronts, we consider the regime close to the Maxwell point and assume that the two fronts are sufficiently separated, that is,

$$u(t,\tau) = u_+(\tau - \Lambda + d/2) + u_-(\tau - \Lambda - d/2) - \sqrt{\mu} + w, \quad (8)$$

where $d = d(t)$ and $\Lambda = \Lambda(t)$ account for the width and centroid between well-separated fronts ($d(t)\sqrt{\mu} \gg 1$) as indicated in Fig. 2(c) such that the distance between the fronts d is greater than the typical size of the core of fronts $1/\sqrt{\mu}$. We add to the superposition of the two fronts, the asymptotic value of the fronts ($\sqrt{\mu}$) and a small perturbation function $w = w(\tau, \Lambda, d)$, with $w \ll 1$. Replacing the previous ansatz (8) in Eq. (4) and linearizing in w, we get

$$\begin{aligned} &-\left[\mu - 3(u_+ + u_- - \sqrt{\mu})^2 + \partial_{zz}\right] w \\ &= \dot{\Lambda}(\partial_z u_+ + \partial_z u_-) - \frac{\dot{d}}{2}(\partial_z u_+ - \partial_z u_-) + \mu\left(u_+ + u_- - \sqrt{\mu}\right) \\ &\eta - \left(u_+ + u_- - \sqrt{\mu}\right)^3 + \partial_{zz} u_+ + \partial_{zz} u_- \\ &+ \alpha\gamma \int_{-\infty}^{\tau} e^{-\alpha(\tau-\tau')}\left(u_+ + u_- - \sqrt{\mu}\right) d\tau', \end{aligned} \quad (9)$$

where the symbol ∂_z accounts for the partial derivative with respect to the argument of the respective function. The above equation corresponds to a linear equation for w, where the equations for Δ and d are unknown.

From Eq. (9), we can derive one equation describing the velocity of the pulse centroid, and another one for the front interaction and locking. In the following, we show the main step of such derivations.[20]

Considering the standard inner product $\langle f|g\rangle = \int_{-\infty}^{\infty} fg\, d\tau$, the linear operator $\mathscr{L} \equiv \mu - 3(u_+ + u_- - \sqrt{\mu})^2 + \partial_{zz}$ is self-adjoint (i.e., $\mathscr{L} = \mathscr{L}^\dagger$). This operator has two specific modes $|T\rangle \equiv \partial_z u_+ + \partial_z u_-$ and $|I\rangle \equiv \partial_z u_+ - \partial_z u_-$ corresponding to translational and interaction mode, respectively. Furthermore, these modes are orthogonal $\langle T|I\rangle = 0$ by simple symmetry arguments. When fronts are far apart, the self-adjoint operator $\mathscr{L}^\dagger$ tends to have two elements in the kernel, the translation mode, and the interaction mode, $\mathscr{L}^\dagger|I\rangle \approx 0$ and $\mathscr{L}^\dagger|T\rangle = 0$. Notwithstanding, the translation mode is always an element of the kernel.

Let us first obtain the equation describing the speed of the pulse centroid. To do so, we multiply the equation by the translation mode $|T\rangle$ and integrate the resulting equation considering symmetry properties. Proceeding in this way, we eventually get

$$\begin{aligned} &\dot{\Lambda}\langle T|\partial_z u_+ + \partial_z u_-\rangle = \dot{\Lambda}\langle T|T\rangle \\ &= \alpha\gamma \int_{-\infty}^{\infty} d\tau\, T(\tau) \int_{-\infty}^{\tau} e^{-\alpha(\tau-\tau')}\left(u_+ + u_- - \sqrt{\mu}\right) d\tau'. \end{aligned} \quad (10)$$

To calculate the integral in the previous equation, we use the approximation

$$u_+ + u_- - \sqrt{\mu} = \begin{cases} -\sqrt{\mu} & \tau \leqslant \Lambda - \dfrac{d}{2}, \\ \sqrt{\mu} & \Lambda - \dfrac{d}{2} < \tau < \Lambda + \dfrac{d}{2}, \\ -\sqrt{\mu} & \tau \geqslant \Lambda + \dfrac{d}{2}. \end{cases} \quad (11)$$

Replacing expression (11) in Eq. (10), integrating into the respective regions where the approximation is constant, and using symmetry arguments, we obtain the following equation the pulse centroid (i.e., its speed):

$$\dot{\Lambda} = v \equiv \frac{2\gamma\sqrt{\mu}}{||T||^2} \int_{-\infty}^{\infty} \partial_z u_+ e^{-\alpha|\tau|}\, d\tau, \quad (12)$$

where $||T||^2 \equiv \langle T|T\rangle$. The integral in Eq. (12) does not depend on Λ, and, therefore, the pulse centroid moves with constant speed v. Numerical simulations show that the pulse spreads with constant speed and confirm the validity of Eq. (12). Figure 3(a) shows a comparison between the above formula and numerical evolution of pulse solution of model Eq. (4). Hence, we can conclude that the moving LSs speed is well described by the expression (12).

To derive the equation describing the interaction of fronts, we follow a procedure similar to the previous one, that is, we multiply Eq. (9) by the interaction mode $|I\rangle$, and then integrate it taking into account symmetry properties, considering that $u_\pm$ are stationary solutions of Eq. (4). Proceeding in this way, we obtain

$$\begin{aligned} \frac{\dot{d}}{2}\langle I|\partial_z u_+ + \partial_z u_-\rangle &= \frac{\dot{d}}{2}||I||^2 = \langle \partial_z u_+ - \partial_z u_-|\eta\rangle \\ &+ -3\langle I|(u_+ - \sqrt{\mu})(u_- - \sqrt{\mu})(u_+ + u_-)\rangle \\ &+ \alpha\gamma \int_{-\infty}^{\infty} d\tau I(\tau) \int_{-\infty}^{\tau} e^{-\alpha(\tau-\tau')}\left(u_+ + u_- - \sqrt{\mu}\right) d\tau'. \end{aligned} \quad (13)$$

Replacing approximation (11) in Eq. (13) and integrating into the respective regions, we obtain, after considering symmetry arguments, the following front interaction law:

$$\dot{d} = a - be^{-2\sqrt{2\mu}d} + c\, e^{-\alpha d}, \quad (14)$$

where

$$a \equiv 2\eta \frac{\int_{-\infty}^{\infty} \partial_z u_+ d\tau}{||I||^2}, \quad (15)$$

$$b \equiv 6\sqrt{\mu} \frac{\int_{-\infty}^{\infty} e^{-\sqrt{2\mu}\tau}(u_- - \sqrt{\mu}) u_- \partial_z u_- d\tau}{\int_{-\infty}^{\infty} (\partial_z u_-)^2\, d\tau}, \quad (16)$$

$$c \equiv \frac{2\gamma\sqrt{\mu}}{||I||^2} \int_{-\infty}^{\infty} \partial_z u_+ e^{-\alpha\tau}\, d\tau. \quad (17)$$

Kinetic equation [i.e., Eq. (14)] governing the time evolution of the LSs width d contains three contributions: the first term on the right side is constant that accounts for the energy difference between the states,

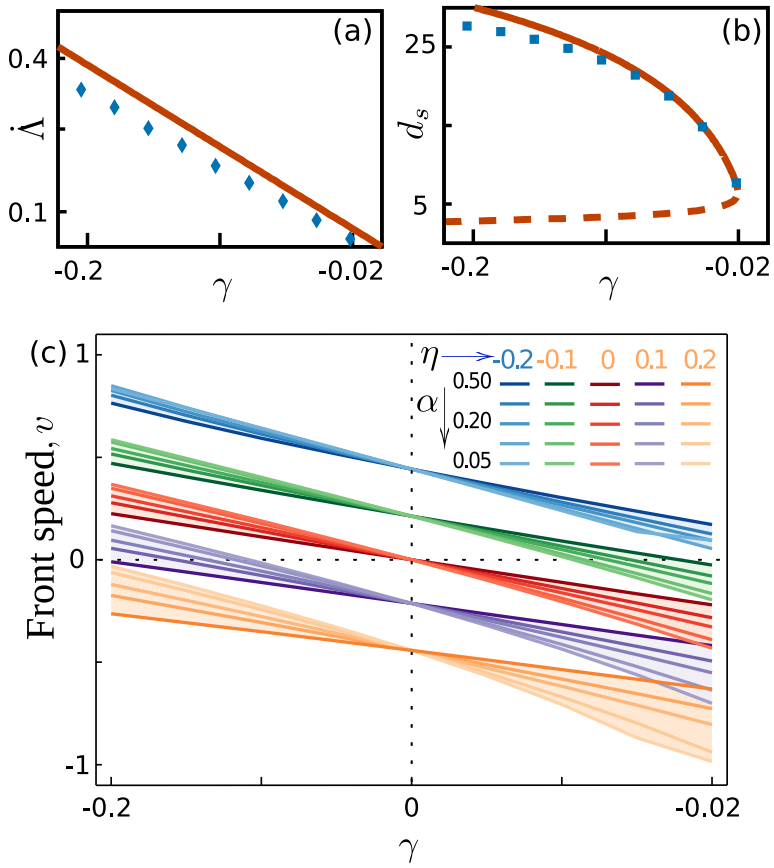

FIG. 3. The speed and the width of moving localized structures of the bistable model with nonlocal time-delayed Eq. (4) by $\alpha = 0.1$, $\mu = 1$, and $\eta = -0.03$. (a) Speed of moving localized structures as a function of the strength of nonlocal coupling γ. The diamonds and continuous curve are the speed obtained numerically and analytically using formula (12). (b) Width of moving localized structures as a function of the strength of nonlocal coupling γ. The square symbols, dashed, and continuous curve are obtained by numerical simulation of model Eq. (4) and numerically solving formula (18). (c) Front speed as a function of the strength of the Raman effect for different values of γ and α.

which is proportional to η; the second term describes the interaction between fronts generated by the effect of the tail, which is always attractive since b is positive; and the last term is attributed to the Raman effect, which is, on the contrary, always repulsive because c is positive.

The fronts lock at the stationary separations d_s satisfying the equation

$$a - be^{-2\sqrt{2\mu}d_s} + ce^{-\alpha d_s} = 0, \tag{18}$$

which, despite its simplicity, does not support explicit analytical solutions. For this reason, we characterize the pulse width and speed numerically and show the main results in Fig. 3(b). We find that the system has two solutions, one stable and one unstable created by means of a saddle-node bifurcation. In order to understand the origin of this instability, we numerically calculated $\dot{d}$ as a function of the width d for a fixed value of either η [see Fig. 4(a)], or γ parameters [see Fig. 4(d)]. The profile of unstable (stable) LSs having a large (small) width is plotted in Fig. 4(b) [Fig. 4(c)]. Figures 4(a) and 4(d) have been obtained from direct simulations of the nonlocal bistable model (4) and using Eq. (14). Indeed, these two results show an excellent agreement. From this perspective, we could say that the moving LSs appear through a saddle-node bifurcation.

Despite the complexity of the nonlocal bistable model (4), the dynamics of moving LSs can be described by the set of simple coupled Eqs. (12) and (14). Note that the interaction of fronts describes coarse LSs since it requires the condition $d(t)\sqrt{\mu} \gg 1$.

IV. BIFURCATION STRUCTURE OF LOCALIZED STATES

In the Kerr cavity nonlinear optics, LSs can be classified into two categories. When the cavity is operating in the anomalous dispersion regime, and close to the subcritical modulational instability (MI), the resulting temporal LSs undergo homoclinic snaking.[4,45–48] In this case, the bifurcation diagram consists of two snaking curves: one describing LSs with odd number of peaks and the other related to those with an even number of peaks. In that case, the formation of LSs do not require HSS bistability, and they can arise in the monostable regime.[2,49] However, when the optical cavity is operating in the normal dispersion regime, HSSs are stable with respect to the MI. In this case, the interaction between switching waves and fronts connecting the two stable HSS u_b and u_t stabilizes dark LSs.[50,51]

In this section, we investigate the effect of the Raman nonlocal delayed response on the bifurcation structure of LSs. The study presented here provides information about the origin, in terms of bifurcations, existence, and stability of the different types of states

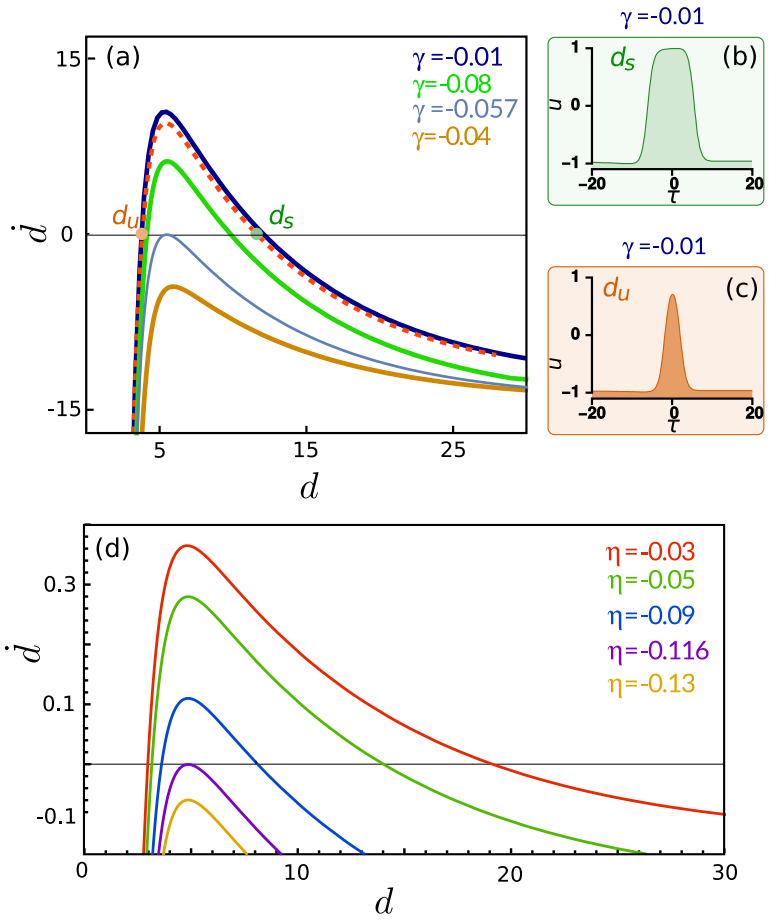

FIG. 4. Panel (a) shows the front interaction Eq. (14) for $\eta = -0.03$ and several values of γ. Solid and dashed curves account for the instantaneous rate of variation of $\dot{d}$ as a function of d obtained using Eq. (14) and by direct simulations of the non-local bistable model Eq. (4). Panels (b) and (c) show the stable (d_s) and the unstable (d_u) moving LSs, respectively. Panel (d) shows the front interaction law (14) for $\gamma = -0.2$ and different values of η. This diagram corresponds to the bifurcation diagram shown in Fig. 5. In both cases, we chose $\alpha = 0.1$ and $\mu = D = 1$.

arising in the system. To do so, it is convenient to define a frame moving at speed v of the LS. By introducing the transformation $\tau \to x = \tau - vt$ and setting $\partial_t u = 0$ in Eq. (4), we obtain

$$\eta + \mu u - u^3 + v\partial_x u + D\partial_x^2 u + \gamma\alpha \int_0^\infty e^{-\alpha(x-s)} u(s)\, ds = 0. \quad (19)$$

In this new frame, the LS appears stationary, and we can track them numerically as a function of a given parameter (e.g., η). The result is shown in the bifurcation Fig. 5. The continuation algorithm is based on a predictor–corrector method,[51,52] which allows us to calculate not only the stable but also the unstable LSs as a function of η. Together with the LS profile, we have to compute its speed, and to do so an extra constraint $C(u) = 0$ must be considered in the calculation. Here, we force the maximum of LS to be at a fixed position x_* by defining

$$C(u) = \left(\frac{du}{dx}\right)_{x_*} = 0. \quad (20)$$

Note that more elaborated phase constraints can be also implemented.[52] To start with the computation, we consider a LS state obtained previously by numerical integration of Eq. (4).

The diagram plotted in Fig. 5 shows L_1-norm of the LS solutions

$$||u||_{L_1} = \frac{1}{L}\int_{-L/2}^{L/2} u(x)\, dx,$$

as a function of η, and we fix the rest of the parameters to $\gamma = -0.2, \alpha = 0.1$, and $\mu = D = 1$. For the domain length, we fix $L = 100$. The green lines in Fig. 5 represent the HSS solution branches u_t, u_m, and u_b, where stable (unstable) branches are plotted using solid (dashed) lines. The blue lines are those corresponding to the LSs, and we use the same criterion for the stability. To obtain the linear stability of the LSs, we calculate the eigenvalues and eigenfunctions of the linear operator associated with (19). Some representative examples of LSs along the bifurcation diagram are shown in panels (i)–(vi). The symmetry of the diagram is a result of the invariance of Eq. (4) under the transformation $(\eta, u) \to -(\eta, u)$. A small amplitude LS like the one depicted in (i) arise unstable from SN_b, increases its amplitude while decreasing η, and becomes stable after passing the fold SN^I [see (ii)]. By increasing again η the structure develops a plateau corresponding to the HSS u_t [see (iii)]. Further increasing η the solution branch collapses to the Maxwell

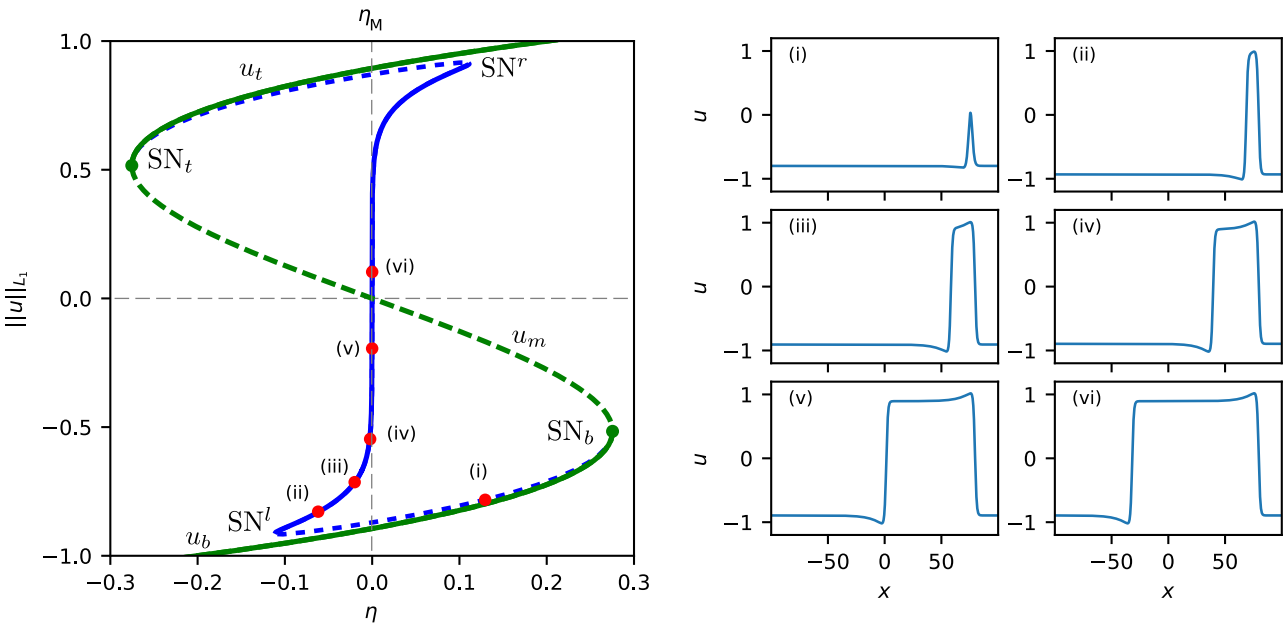

FIG. 5. Bifurcation diagram associated with the LSs formed through front locking. The green lines correspond to the HSS solution and those in blue are the LSs solution branches. Some examples of the modification of the LSs along the diagram are shown in panels (i)–(vi). Stable (unstable) solutions are marked using solid (dashed) lines. $SN_{b,t}$ correspond to the fold of the HSS, and $SN^{l,r}$ are the saddle-node bifurcation of the LSs. The Maxwell point η_M of the system is marked using a dashed gray vertical line. Here, we consider $\gamma = -0.2$, $\alpha = 0.1$, $\mu = D = 1$, and $L = 100$.

point of the system η_M where the LS broadens until reaching the limits of the domain. At this stage, the same process repeats for a LS related with the previous one by the inversion $u \to -u$.

The bifurcation diagram shown in Fig. 5 is a direct consequence of the front interaction and locking described by Eqs. (14) and (18), respectively. For a η value between SN^l and η_M, Eq. (14) shows two equilibria, solutions of Eq. (18), namely, d_u, which is unstable, and d_s which is stable [see Fig. 4(d)]. These two equilibria correspond, respectively, to the dashed and solid blue lines in Fig. 5. Increasing $|\eta|$, d_u and d_s approach each other until they, eventually, collide in the saddle-node bifurcation SN^l. This collision occurs when the maximum of the curve shown in Fig. 4(d) becomes tangent to $\dot{d} = 0$. Bellow this point no LSs exist. Increasing $|\eta|$, the separation of d_u and d_s increases exponentially, and with it their norm difference [see Fig. 5]. As a result, the stable branch of LSs approaches asymptotically η_M. The description of the bifurcation diagram around SN^r follows the same reasoning. As a consequence, LSs remain stable all along the Maxwell point in-between SN_b and SN_t.

This bifurcation scenario shares some similarities with the *collapsed snaking* reported in previous works,[41–44] where LSs possess damped oscillatory tails. This type of bifurcation structure has been also characterized following a front interaction approach in various contexts.[53–56]

To complete the diagram plotted in Fig. 5, we show how the width d of the structure (at half of its maximum) modifies with η [see Fig. 6(a)]. Figure 6(b) shows the velocity as a function of

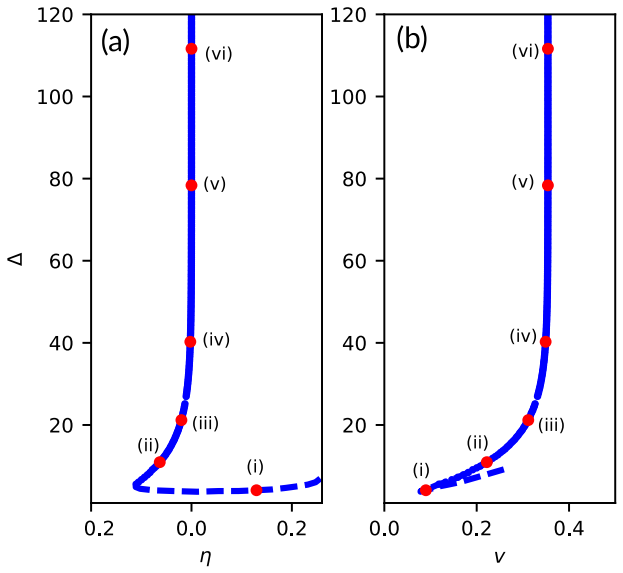

FIG. 6. In (a), we plot the same bifurcation diagram than in Fig. 5 but showing the width d of the LS as a function of η. In (b), we plot the width vs the velocity v of the LSs. The vertical dashed line in (a) shows the Maxwell point η_M.

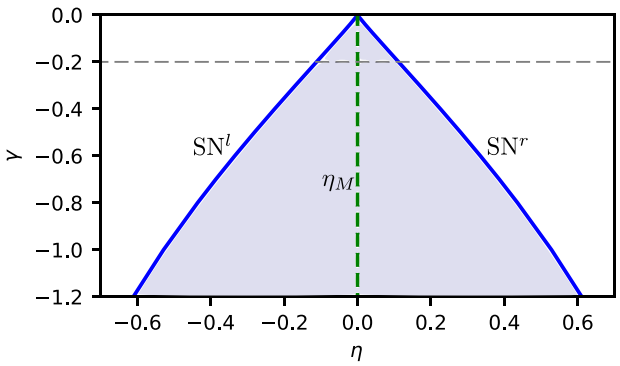

FIG. 7. Phase diagram in the (η, γ)—parameter space, showing the main bifurcations lines of the system, namely, η_M, SN^l, and SN^r. The horizontal dashed gray line corresponds to the diagrams shown in Figs. 5 and 6. Here $\alpha = 0.1$, $\mu = D = 1$.

d. Comparing both panels, we can observe that v increases with d and saturates to a constant value at the Maxwell point of the system η_M.

Figure 7 shows the phase diagram in the $(\eta, \gamma)-$ parameter space for a fixed values of α, and $\mu = D = 1$, where SN^l and SN^r are plotted in blue, and the Maxwell point η_M in green. The light gray shadowed area corresponds to the region of existence of LSs, and the horizontal gray line to the bifurcation diagrams shown in Figs. 5 and 6 for $\gamma = -0.2$. The $\eta \to -\eta$ symmetry of the system is also reflected in this phase diagram, where the left (right) part corresponds to the bottom (top) part of the diagram shown in Fig. 5. Localized structures persist when modifying the strength of the nonlocal delay response $|\gamma|$. Decreasing $|\gamma|$, $SN^{l,r}$ approach one another until they collide with the η_M at $\gamma = 0$. At this point, the LSs disappear. Increasing $|\gamma|$, however, the region of existence of the LSs broadens as $SN^{l,r}$ separate from η_M. This result is consistent with the one predicted by Eq. (18).

V. CONCLUSION

We have considered an optical resonator filled with a Kerr medium such as fibers with a Raman nonlocal delay response. Normal dispersion regime has been investigated where HSS are stable with respect to the modulational or Turing type of instabilities. We have focused our analysis on a regime close to the critical point associated with bistability where the dynamics is described by a generic bistable model. In this regime, moving temporal LSs resulting from front interaction are described in a more detailed way with respect to recent investigations of this issue.[20] Through front interaction, we have characterized these structures by deriving their shape, width, and speed. We have shown that front interaction modifies drastically the dynamics of bistable systems. The nonlocal delay effect is originated from temporal correlations that are inherent not only to optical and magnetic systems but also relevant to biological systems. This study is obviously relevant to other nonlinear systems with a nonlocal time delay. The normal form reduction of the problem makes our analysis very general and one may expect that moving temporal LSs constitute a dominant dynamical behavior in many out of equilibrium systems. One may expect that, owing to its general character, the moving states reported in our analysis may, therefore, be observed experimentally. We have characterized the moving LSs by computing their bifurcation structure and stability. This analysis has revealed that the nature of the bifurcation structure belongs to a class similar to the collapsed snaking type.

To understand the bifurcation structure, dynamics, and stability of moving temporal LSs, we have followed two complementary approaches: one analytical describing the front interaction and locking, and the other numerical to characterize stationary LSs and their stability.

Further investigations are necessary to clarify the interaction between two or more moving LSs, as well as the effect of noise on front propagation.[57] Front interaction under the combined influence of the noise and the Raman response will be a subject of future works.

ACKNOWLEDGMENTS

This research was funded by the Millennium Institute for Research in Optics (MIRO) and FONDECYT Projects (No. 1180903). M.T. and P.P.-R. received support from the Fonds National de la Recherche Scientifique (Belgium). S.C. acknowledges the LABEX CEMPI (No. ANR-11-LABX-0007) as well as the Ministry of Higher Education and Research, Hauts de France council and European Regional Development Fund (ERDF) through the Contract de Projets Etat-Region (CPER Photonics for Society P4S).

This contribution is devoted to honoring Professor Enrique Tirapegui on the occasion of his 80th anniversary.

DATA AVAILABILITY

The data that support the findings of this study are available from the corresponding author upon reasonable request.

REFERENCES

[1] L. A. Lugiato and R. Lefever, Phys. Rev. Lett. **58**, 2209 (1987).
[2] A. J. Scroggie, W. J. Firth, G. S. McDonald, M. Tlidi, R. Lefever, and L. A. Lugiato, Chaos Solitons Fractals **4**, 1323 (1994).
[3] F. Leo, S. Coen, P. Kockaert, S. P. Gorza, P. Emplit, and M. Haelterman, Nat. Photon. **4**, 471 (2010).
[4] S. Coen, M. Tlidi, P. Emplit, and M. Haelterman, Phys. Rev. Lett. **83**, 2328 (1999).
[5] V. Odent, M. Tlidi, M. G. Clerc, P. Glorieux, and E. Louvergneaux, Phys. Rev. A **90**, 011806(R) (2014).
[6] Z. Liu, M. Ouali, S. Coulibaly, M. G. Clerc, M. Taki, and M. Tlidi, Opt. Lett. **42**, 1063 (2017).
[7] K. Panajotov, M. G. Clerc, and M. Tlidi, Eur. Phys. J. D **76**, 176 (2017).
[8] N. Akhmediev *et al.*, J. Opt. **18**, 063001 (2016).
[9] S. Coulibaly, M. Taki, A. Bendahmane, G. Millot, B. Kibler, and M. G. Clerc, Phys. Rev. X **9**, 011054 (2019).
[10] L. A. Lugiato, F. Prati, and M. Brambilla, *Nonlinear Optical Systems* (Cambridge University Press, 2015).
[11] Y. K. Chembo, D. Gomila, M. Tlidi, and C. R. Menyuk, "Theory and applications of the Lugiato-Lefever equation," Eur. Phys. J. D **71**, 299 (2017).
[12] M. Tlidi, K. Staliunas, K. Panajotov, A. G. Vladimirov, and M. G. Clerc, Philos. Trans. R. Soc. A **372**, 20140101 (2014).
[13] *Nonlinear Dynamics: Materials, Theory and Experiments*, edited by M. Tlidi and M. G. Clerc (Springer Proceedings in Physics, 2016), Vol. 173.

[14]M. G. Clerc, M. A. Ferré, S. Coulibaly, R. G. Rojas, and M. Tlidi, Opt. Lett. **42**, 2906 (2017).
[15]T. W. Hansch, Rev. Mod. Phys. **78**, 1297 (2006).
[16]P. Del'Haye, A. Schliesser, O. Arcizet, T. Wilken, R. Holzwarth, and T. J. Kippenberg, Nature **450**, 1214 (2007).
[17]T. J. Kippenberg, R. Holzwarth, and S. A. Diddams, Science **332**, 555 (2011).
[18]F. Ferdous, H. Miao, D. E. Leaird, K. Srinivasan, J. Wang, L. Chen, L. T. Varghese, and A. M. Weiner, Nat. Photon. **5**, 770 (2011).
[19]Y. K. Chembo, I. S. Grudinin, and N. Yu, Phys. Rev. A **92**, 043818 (2015).
[20]M. G. Clerc, S. Coulibaly, and M. Tlidi, Phys. Rev. Res. **2**, 013024 (2020).
[21]M. Tlidi, A. G. Vladimirov, D. Pieroux, and D. Turaev, Phys. Rev. Lett. **103**, 103904 (2009).
[22]K. Panajotov and M. Tlidi, Eur. Phys. J. D **59**, 67 (2010).
[23]M. Tlidi, K. Panajotov, M. Ferré, and M. G. Clerc, Chaos **27**, 114312 (2017).
[24]N. Bloembergen, *Nonlinear Optics* (World Scientific, 1996).
[25]G. P. Agrawal, *Nonlinear Fiber Optics* (Springer, Berlin, Heidelberg, 2000).
[26]L. D. Landau and E. M. Lifshitz, *Electrodynamics of Continuous Media*, Course of Theoretical Physics Vol. 8 (Oxford, 1960).
[27]A. Hutt, Phys. Rev. E **70**, 052902 (2004).
[28]S. Coombes, Biol. Cybern. **93**, 91 (2005).
[29]F. M. Atay and A. Hutt, SIAM J. Appl. Dyn. Syst. **5**, 670 (2006).
[30]J. D. Murray, *Mathematical Biology* (Springer-Verlag, New York, 2001).
[31]L. A. Lugiato, F. Prati, M. L. Gorodetsky, and T. J. Kippenberg, Philos. Trans. R. Soc. A **376**, 20180113 (2018).
[32]M. Tlidi, M. Clerc, and K. Panajotov, Philos. Trans. R. Soc. A (Lond.) **376**, 20180114 (2018).
[33]K. J. Blow and D. Wood, IEEE J. Quantum Electron **25**, 2665 (1989).
[34]Q. Lin and G. P. Agrawal, Opt. Lett. **31**, 3086 (2006).
[35]M. Tlidi, L. Bahloul, L. Cherbi, A. Hariz, and S. Coulibaly, Phys. Rev. A **88**, 035802 (2013).
[36]P. Parra-Rivas, D. Gomila, and L. Gelens, Phys. Rev. A **95**, 053863 (2017).
[37]A. G. Vladimirov, S. V. Gurevich, and M. Tlidi, Phys. Rev. A **97**, 013816 (2018).
[38]A. Hariz, L. Bahloul, L. Cherbi, K. Panajotov, M. Clerc, M. A. Ferré, B. Kostet, E. Averlant, and M. Tlidi, Phys. Rev. A **100**, 023816 (2019).
[39]O. Descalzi, J. Cisternas, and H. R. Brand, Phys. Rev. E **100**, 052218 (2019).
[40]O. Descalzi and H. R. Brand, Chaos **30**, 043119 (2020).
[41]J. Knobloch and T. Wagenknecht, Physica D **206**, 82 (2005).
[42]A. Yochelis, J. Burke, and E. Knobloch, Phys. Rev. Lett. **97**, 254501 (2006).
[43]P. Parra-Rivas, E. Knobloch, D. Gomila, and L. Gelens, Phys. Rev. A **93**, 063839 (2016).
[44]P. Parra-Rivas, L. Gelens, and F. Leo, Phys. Rev. E **100**, 032219 (2019).
[45]D. Gomila, A. J. Scroggie, and W. J. Firth, Physica D **227**, 70 (2007).
[46]M. Tlidi and L. Gelens, Opt. Lett. **35**, 270 (2010).
[47]P. Parra-Rivas, D. Gomila, M. A. Matías, S. Coen, and L. Gelens, Phys. Rev. A **89**, 043813 (2014).
[48]P. Parra-Rivas, D. Gomila, L. Gelens, and E. Knobloch, Phys. Rev. E **97**, 042204 (2018).
[49]M. Tlidi, P. Mandel, and R. Lefever, Phys. Rev. Lett. **73**, 640 (1994).
[50]P. Parra-Rivas, D. Gomila, E. Knobloch, S. Coen, and L. Gelens, Opt. Lett. **41**, 2402 (2016).
[51]E. Doedel, H. B. Keller, and J. P. Kernevez, Int. J. Bifurc. Chaos **1**, 493 (1991).
[52]E. Doedel, H. B. Keller, and J. P. Kernevez, Int. J. Bifurc. Chaos **1**, 745 (1991).
[53]P. Coullet, C. Elphick, and D. Repaux, Phys. Rev. Lett. **58**, 431 (1987).
[54]P. Coullet, Int. J. Bifurc. Chaos **12**, 2445 (2002).
[55]M. G. Clerc, D. Escaff, and V. M. Kenkre, Phys. Rev. E **72**, 056217 (2005).
[56]M. G. Clerc, D. Escaff, and V. M. Kenkre, Phys. Rev. E **82**, 036210 (2010).
[57]M. G. Clerc, C. Falcon, and E. Tirapegui, Phys. Rev. Lett. **94**, 148302 (2005).